Electronic Supplementary Material (ESI) for Journal of Materials Chemistry A.
This journal is © The Royal Society of Chemistry 2019

Supporting information

Bimetallic phosphosulfide Zn–Ni–P–S nanosheets as binder-free electrodes for aqueous asymmetric supercapacitors with impressive performance

Xueyan Lei,[a] Shicheng Ge,[b] Yihong Tan,[c] Jing Li,[a] Zhi Wang,[a] Ping Liu,[a] Chao Feng,[a] Bin Xiang[a]*

[a]Hefei National Research Center for Physical Sciences at the Microscale, Department of Materials Science & Engineering, CAS Key Laboratory of Materials for Energy Conversion, University of Science and Technology of China, 230026, Hefei, Anhui, China.

[b]School of Mechanical Engineering, Nanjing University of Science and Technology, 210094, Nanjing, China.

[c]Department of Applied Chemistry, University of Science and Technology of China, 230026, Hefei, Anhui, China.

*Corresponding author: binxiang@ustc.edu.cn

Note S1. The XRD patterns for the ZNP and ZNS

The diffraction peaks of the ZNP (Fig. S4a) can be well assigned to the phase Ni_2P (JCPDS: PDF# 03−0953), $Ni_{12}P_5$ (JCPDS: PDF# 22−1190) and $Ni(OH)_2$ (JCPDS: PDF# 14−0117). The peaks at 40.7°, 44.4°, 47.3°, 54.1°, 54.9°, 72.7° and 74.6° can be well assigned to the (111), (201), (210), (300), (211), (311), and (400) planes of the Ni_2P, respectively. The peaks at 20.5°, 38.4°, 41.6°, 44.5°, and 48.9°can be well assigned to the (200), (112), (321), (330), and (312) planes of the $Ni_{12}P_5$, respectively. The diffraction peaks at 19.1°, 38.7°, 37.58°, 51.8°, and 59° can be indexed to the respective (001), (101), (102), and (110) planes of the phase $Ni(OH)_2$, respectively. The diffraction peaks of the ZNS correspond to those planes of the phase Ni_3S_2 (JCPDS: PDF# 54−0413) (Fig. S4b). In detail, the diffraction peaks at 21.78°, 31.08°, 37.58°, 38.22°, 44.42°, 49.38°, 50.14°, 54.67°, and 55.3° can be indexed to the respective (101), (012), (003), (021), (202), (113), (211), (104), and (122) planes of the phase Ni_3S_2, respectively.

Note S2. The CV curves at different scanning rates and GCD curves at different current densities for the ZNPS, ZNP and ZNS

The electrochemical signatures shown in Fig. S5a-f clearly evidence redox, faradic behaviors for the ZNPS, ZNP and ZNS with a set of pronounced redox peaks and discharge platforms, indicating that a substantial fraction of the charge storage arises from faradaic redox reactions. When the scanning rates increase from 5 to 25 mV s^{-1} in CV test, we find that the anodic peak potential differences of the ZNPS, ZNP and ZNS are 0.135 V, 0.091 V, 0.133 V, respectively. The cathodic peak potential differences of the ZNPS, ZNP and ZNS are 0.121 V, 0.061 V, 0.078 V, respectively. The deviation value of the ZNPS electrode peak potential is greater. The reason for this phenomenon could be explained as follows: in the 3 M KOH electrolyte solution, when the applied electric field is not provided, the concentration of each part of the electrolyte solution is uniform. After the applied electric field is provided, the first reactant consumed in the electrolyte solution should be OH^- in the liquid layer near the surface of the working electrode. The corresponding electrochemical reactions of the ZNPS electrode could be expressed in the following reaction formula:

$$Ni_2P + 2OH^- \leftrightarrow Ni_2P(OH)_2 + 2e^- \qquad (1)$$

$$Ni_3S_2 + 3OH^- \leftrightarrow Ni_3S_2(OH)_3 + 3e^- \qquad (2)$$

Therefore, the concentration of OH^- in the liquid layer near the surface of the working electrode decreases continuously, which forms a concentration difference with the electrolyte ontology. At this point, the OH^- of electrolyte ontology should diffuse to the surface of the electrode to supplement the concentration difference, so that the concentration tends to be uniform. As the diffusion speed of OH^- cannot keep up with the speed of electrode reaction consumption OH^-, the OH^- concentration in liquid layer near the electrode surface further reduces. The lack of OH^- near the surface of the working electrode makes the electrode potential become positive and polarized.

From the CV curves of the ZNPS, ZNP and ZNS at the same scanning rate of 10 mV s^{-1}, we can find that the redox peaks' current densities of the ZNPS are the largest, indicating that the ZNPS occurred stronger electrochemical reactions than the ZNP and ZNS. Therefore, when the oxidation reactions occur, the OH^- consumption's speed of the ZNPS electrode reaction is higher than that of the ZNP and ZNS electrodes. So the OH^- concentration difference in liquid layer near the ZNPS electrode surface with the electrolyte ontology is more severely due to the finite diffusion speed of OH^-. Therefore, the lack of more OH^- near the surface of the ZNPS electrode makes the electrode potential become more positive.

Instead, when the reduction reactions occur, the OH^- is released in liquid layer near the electrode surface. The ZNPS with stronger electrochemical reactions releases OH^- faster than that of the ZNP and ZNS. While the OH^- in liquid layer near the electrode surface cannot diffuse into the electrolyte ontology in time due to the diffusion speed of OH^- is slower than the release speed of OH^-. Therefore, the OH^- concentration difference in liquid layer near the ZNPS electrode surface with the electrolyte ontology is more severely. Thus, the accumulation of more OH^- near the surface of the ZNPS electrode makes the electrode potential become more negative. Therefore, it is observed more severe polarization in the ZNPS than in the ZNP and ZNS.

Note S3. The Coulomb efficiency (CE) data of the ZNPS, ZNP and ZNS

The Coulomb efficiency (CE) data of all samples is shown in Table S2. It can be seen from Table S2 that the CE of the three materials increases with the increase of current density. At low current density, the CE is lower than that of at higher current density, which could be some irreversible side reactions occurring during the electrochemical redox reaction process, leading to incomplete discharge. As the current density increases, charging and discharging process speeds up. The charging and discharging time decreases. The influence of double-layer capacitor based on ion adsorption/desorption on the electrochemical process increases, so the CE increases.

The reasons why the ZNPS has the lowest CE among three samples for the three-electrode GCD test can be summarized as follows: First, Fig. S1(f), Fig. S1(i), Fig. S1(l) show that three materials have different nanosheets thickness, and the thickness of the ZNPS, ZNP and ZNS nanosheets are approximately 40.63 nm, 31.75 nm, 31.75 nm, on average, respectively. This thickness difference may cause different CE. Second, the mass loading of the ZNPS, ZNP and ZNS materials on substrate are 3.5 mg cm^{-2}, 3 mg cm^{-2}, 3 mg cm^{-2} on average, respectively. The difference of mass loading on substrate may also lead to different CE. The ZNPS with thickest nanosheets and highest mass loading may not be fully infiltrated during the GCD test, leading to smaller ionic diffusion capacity in the electrolyte at the initial stage, thereby lower CE. What’s more, more severe polarization in the ZNPS than in the ZNP and ZNS may also cause lower CE.

Note S4. Electrochemical characteristics of the AC electrode

The CV tests within an operating voltage range from –1 to 0 V at different scanning rates from 5 to 50 mV s^{-1}, GCD tests within an operating voltage range from –1 to 0 V at different current densities from 2 to 10 A g^{-1}, and the EIS test within the frequency range of $0.01-10^5$ Hz at open-circuit voltage of 1200 s were executed to study the electrochemical performance of the AC electrode (Fig. S7a–c). The CV curves (Fig. S7a) exhibit a nearly rectangular shape and the GCD plots (Fig. S7b) of the AC electrode are linear, indicating a typical EDLC behavior. The EIS curve of the AC electrode (Fig. S7c) exhibits a semicircle with a small diameter in the high-frequency region and inclined line with high slope in the low-frequency region, indicating the AC electrode possesses a high electrical conductivity and fast ion diffusion capability. Fig. S7d is the diagram of the relationship between specific capacitance and current density. The AC electrode displays a high specific capacitance of 152.6 F g^{-1} at the current density of 2 A g^{-1} and good rate performance with an initial capacitance retention of 77.33% when the current density increase from 2 to 10 A g^{-1}.

Note S5. The CV curve of the Ni foam

To investigate the contribution of Ni foam to the specific capacity of the as-prepared materials, CV test at a scanning rate of 5 mV s^{-1} was carried out in 3 M KOH electrolyte, as shown in Fig. S10. A pair of redox peaks were observed in the CV curve of Ni foam, which is attributed to the nickel oxide on the surface of the Ni foam. However, the peaks' current densities of Ni foam reach only ~1.02 and 0.71 mA cm^{-2}. It is two orders of magnitude lower than these of the as-prepared ZNPS (~109 and 103 mA cm^{-2}) at the same scanning rate. Therefore, the contribution of the Ni foam to the specific capacity of the as-prepared materials could be neglected.

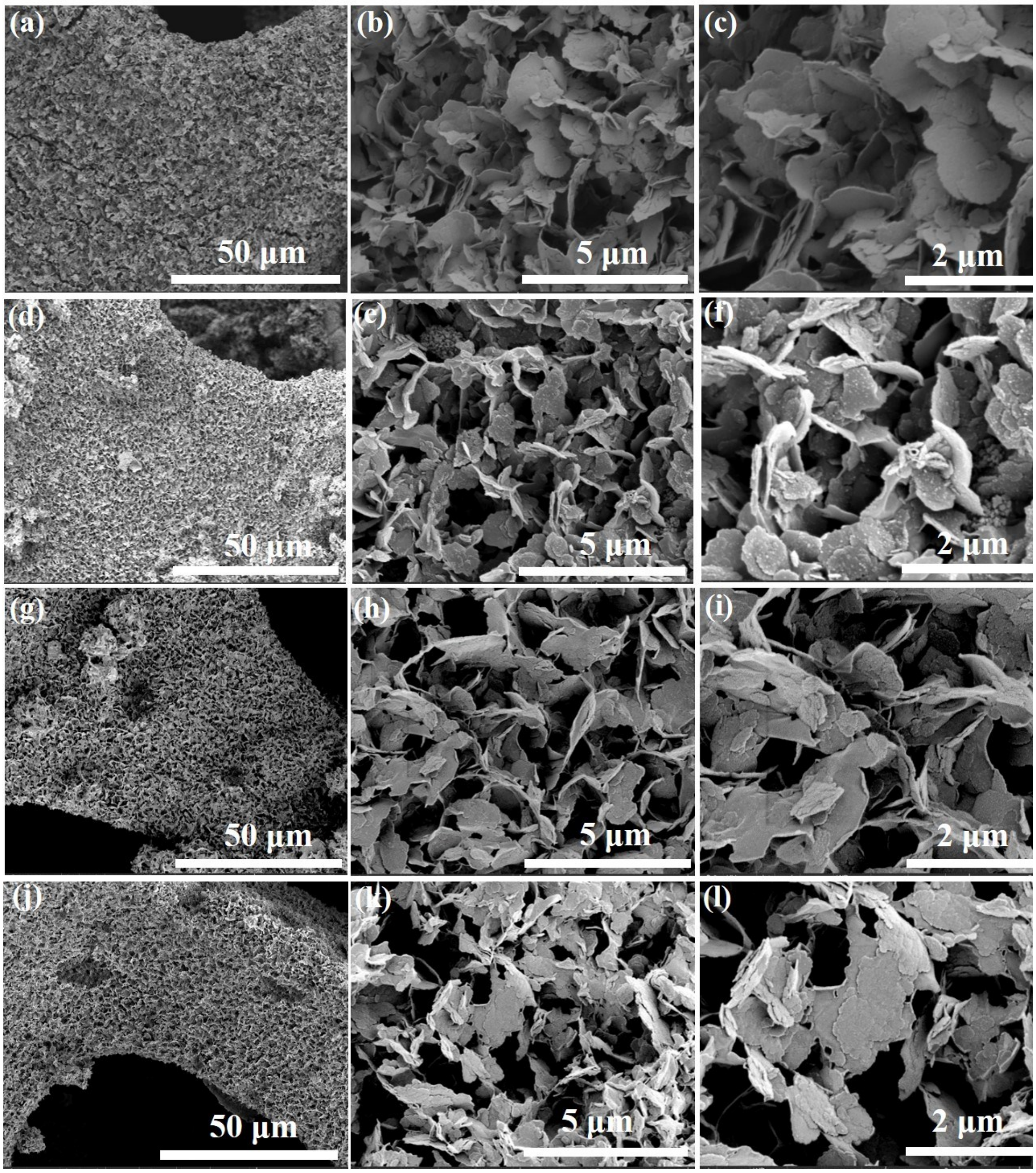

Fig. S1 (a–c) The FESEM images of the Zn–Ni precursors, (d–f) the FESEM images of the ZNPS, (g–i) the FESEM images of the ZNP, and (j–l) the FESEM images of the ZNS.

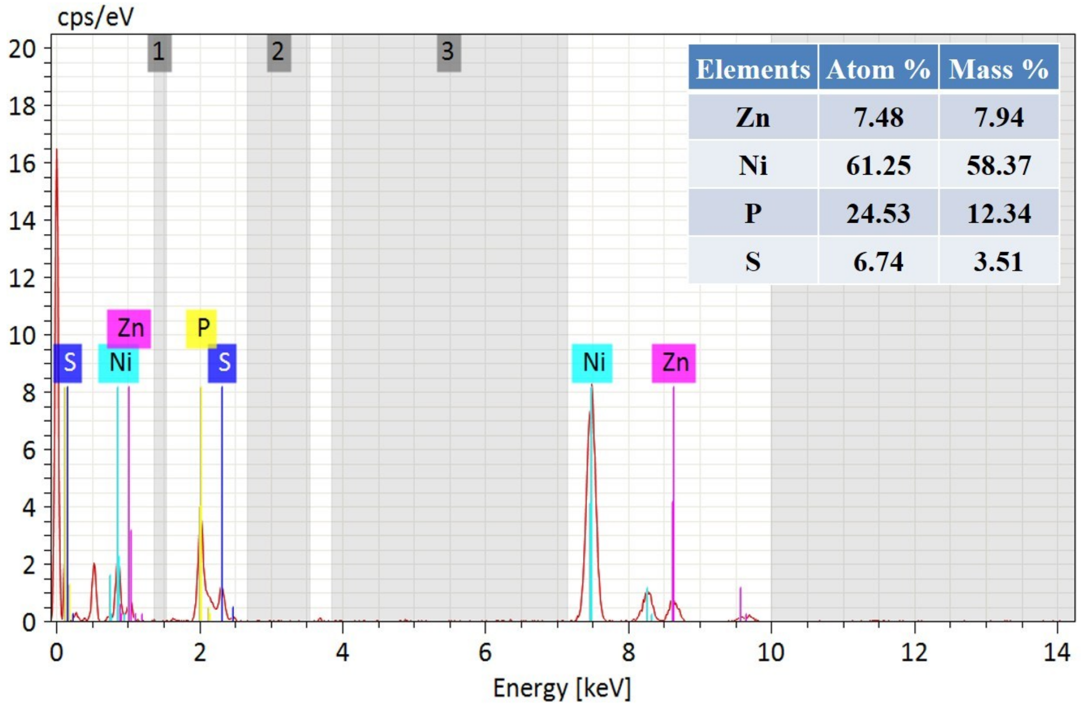

Elements	Atom %	Mass %
Zn	7.48	7.94
Ni	61.25	58.37
P	24.53	12.34
S	6.74	3.51

Fig. S2 (a) The EDS pattern of the ZNPS, the inset shows the corresponding element content.

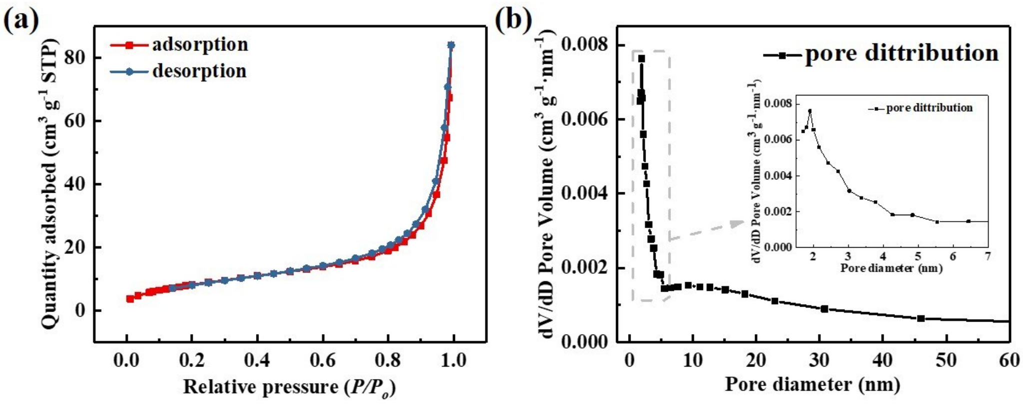

Fig. S3 (a) The N_2 isothermal adsorption/desorption curve of the ZNPS, and (b) the pattern of pore distribution of the ZNPS.

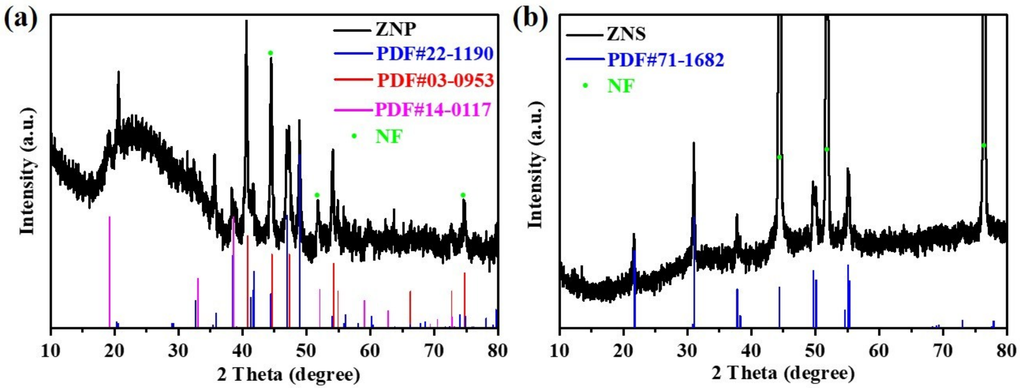

Fig. S4 The XRD patterns of the ZNP (a), and the ZNS (b).

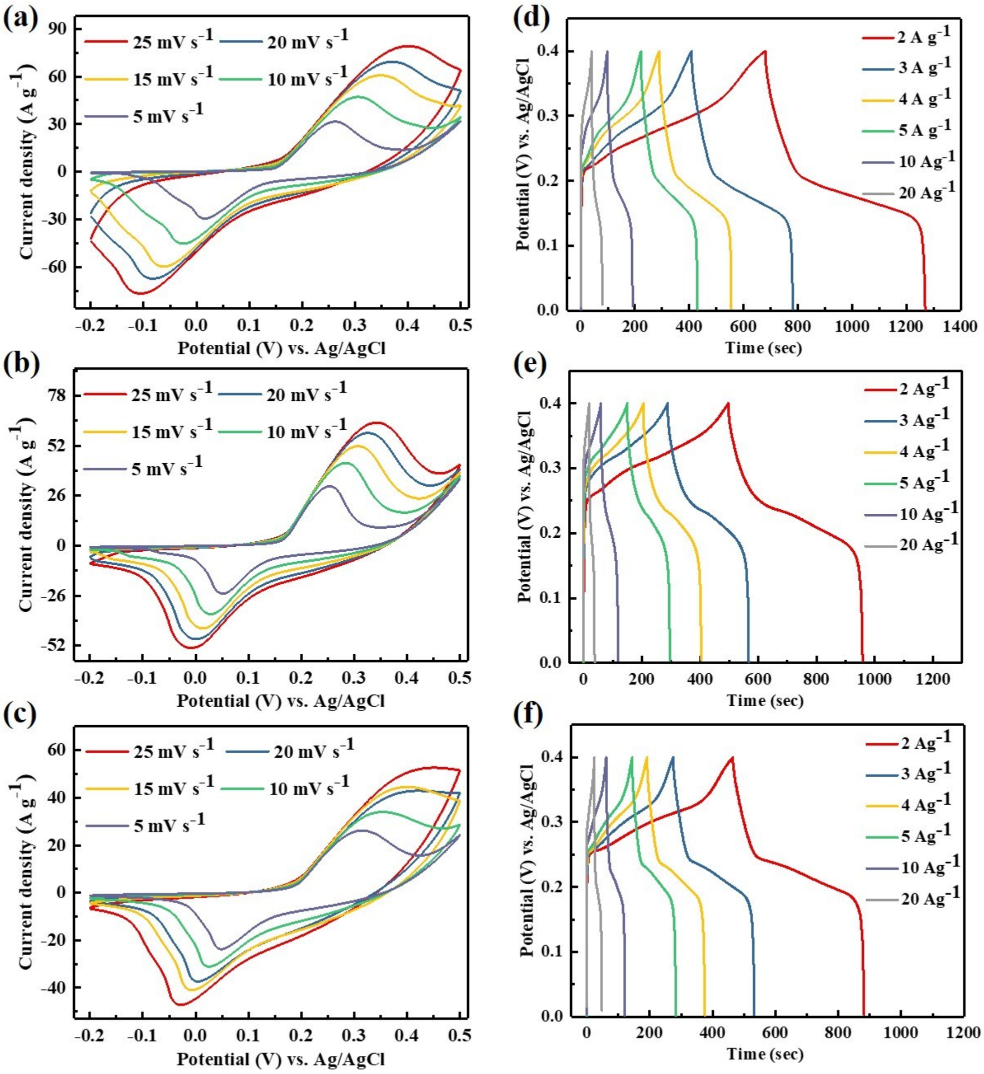

Fig. S5 (a–c) The CV curves of the ZNPS, ZNP and ZNS electrodes at different scanning rates from 5 to 25 mV s^{-1} within a potential range from –0.2 to 0.5 V, and (d–f) the GCD curves of the ZNPS, ZNP and ZNS electrodes at various current densities from 2 to 20 A g^{-1} within a potential range from 0 to 0.4 V.

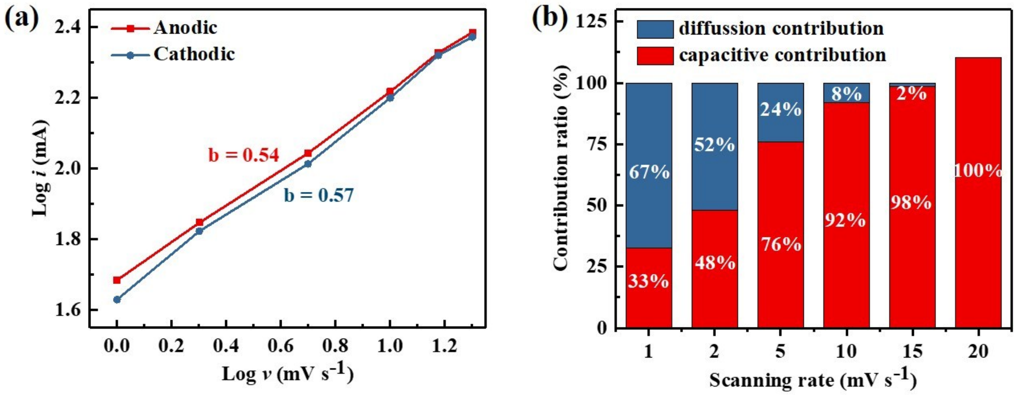

Fig. S6 (a) The plots of log (*v*) versus log (*i)* of the cathodic peak current and anodic peak current, and (b) the percentage split up of capacity into diffusion controlled contribution and capacitive contribution at various scanning rates from 1 to 20 mV s^{-1}.

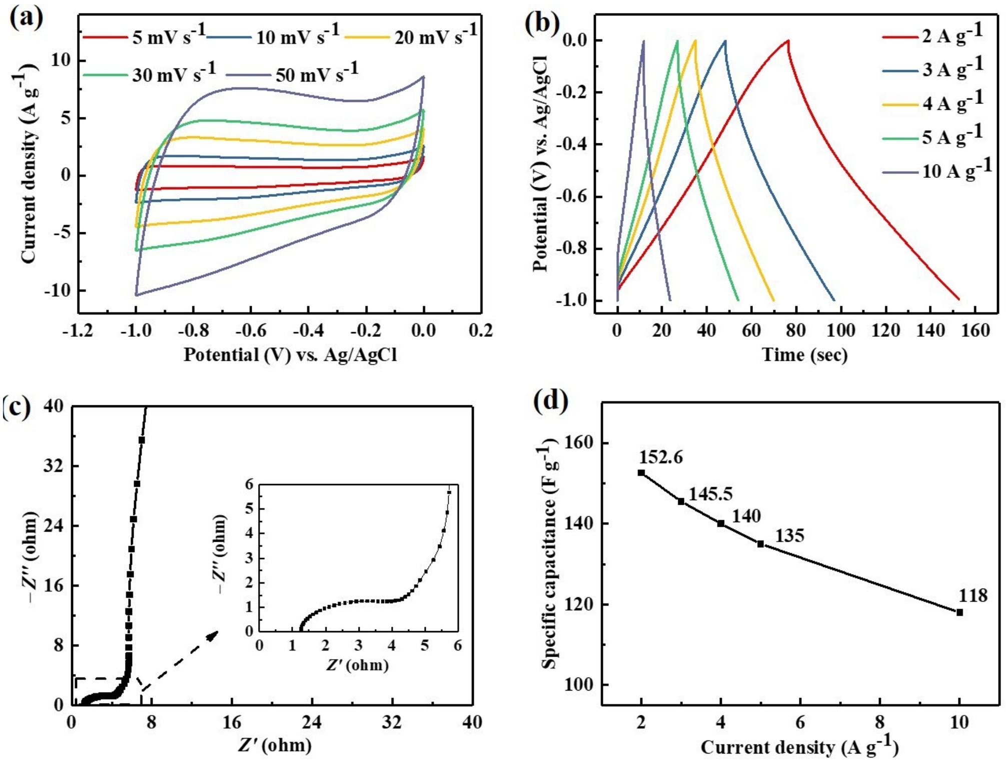

Fig. S7 (a) The CV curves of the AC electrode at different scanning rates from 5 to 50 mV s^{-1} within a potential range from –1 to 0 V, (b) the GCD curves of the AC electrode at different current densities from 2 to 10 A g^{-1} within a potential range from –1 to 0 V, (c) the EIS curve of the AC electrode acquired at open circuit potential, the inset is its enlarged view at high-frequency region, (d) Specific capacitance of the AC electrode at different current densities from 2 to 10 A g^{-1}.

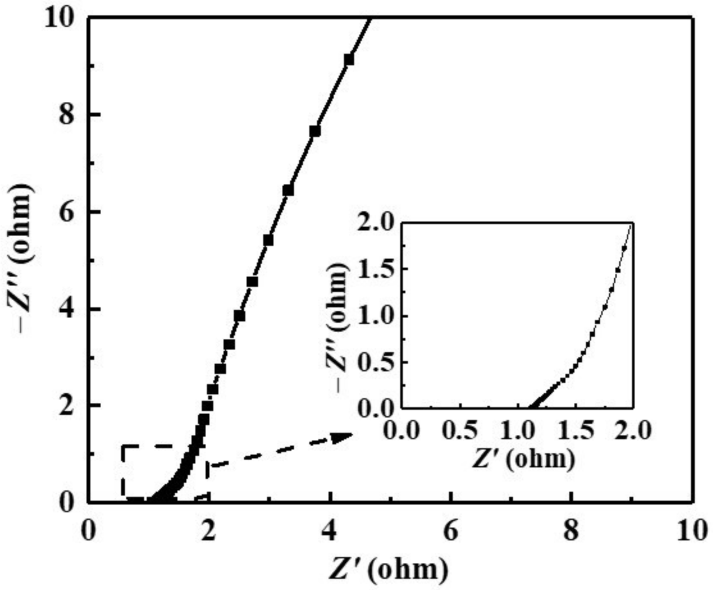

Fig. S8 The EIS curve of ZNPS//AC device acquired at open circuit potential within the frequency range of 0.01−10^5 Hz, the inset is its enlarged view at high frequency region.

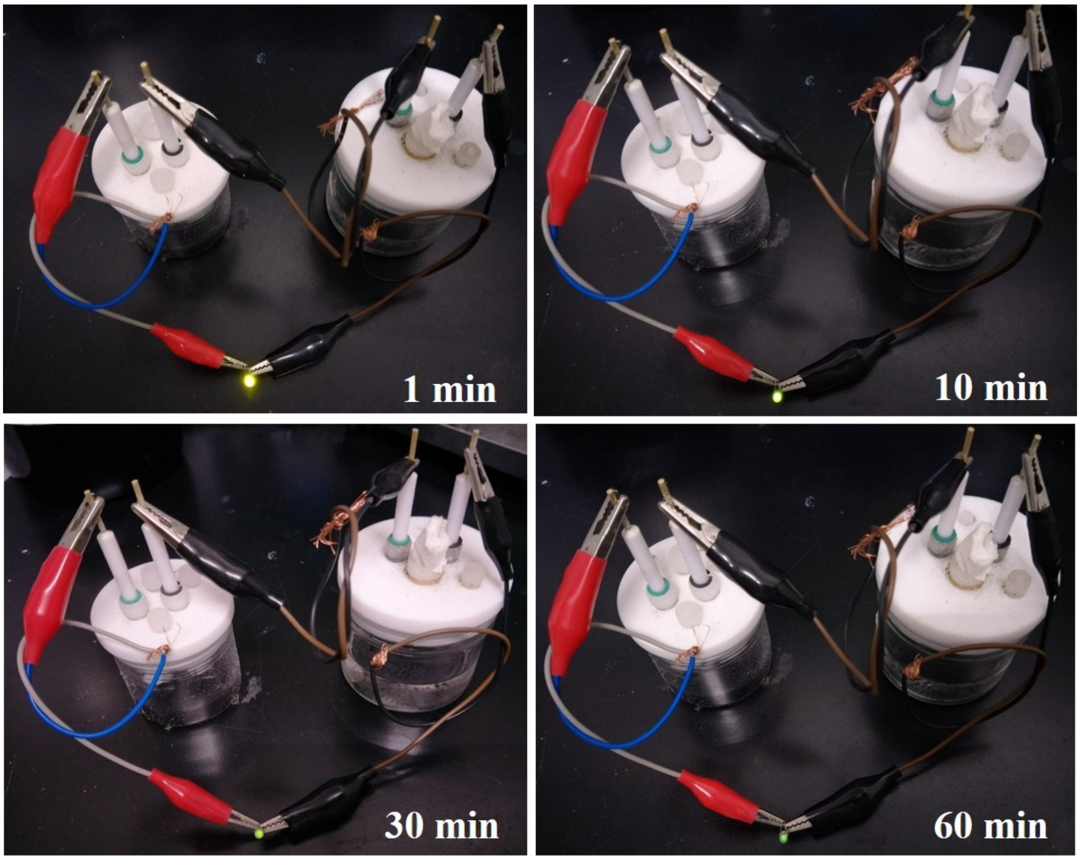

Fig. S9 The photographs of a yellow LED lighted at different running time by two ZNPS//AC devices in series.

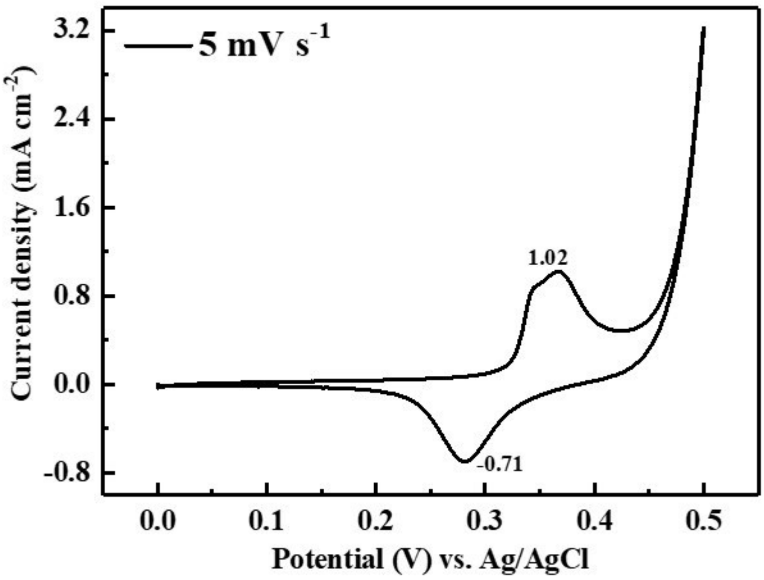

Fig. S10 The CV curve of the Ni foam at a scanning rate of 5 mV s^{-1} in 3 M KOH electrolyte.

Table S1. Capacity performance of the bimetallic phosphosulfide ZNPS in three-electrode system in this work, compared to that of other bimetallic phosphide and bimetallic sulfide electrodes reported in previous literatures

Materials	**Electrolyte**	**Current density ($A\ g^{-1}$)**	**Specific capacity ($F\ g^{-1}$)**	**Refs**
Ni_8-Co_1-P	3 M KOH and 0.5 M LiOH	1	1448	1
		16	1173	
NiCoS	6 M KOH	1	1036	2
		20	705	
Ni_3S_2–$Cu_{1.8}S$	6 M KOH	2	1481.9	3
		10	862.1	
$NiCo_2S_4$@mesocarbon microbead	3 M KOH	1	936	4
$Ni_xCo_{1-x}O/Ni_yCo_{2-y}P$@C	6 M KOH	1	2638	5
$Ni_3S_2/CoNi_2S_4$/NF	6 M KOH	2	2435	6
$Zn_{0.76}Co_{0.24}S$	6 M KOH	2	2484	7
		10	1819.2	
NiCoP/NiCo−OH	6 M KOH	1	1100	8
Ni–Co–S/G	6 M KOH	1	1492	9
NiCo−LDH/NiCoP@NiMn−LDH	1 M KOH	1	2318	10
		20	1400	
S−NiCoP	2 M KOH	2	1080	11
		20	612	
$NiCo_2S_4$	6 M KOH	2.5	2363.1	12
NiCoP@C@$Ni(OH)_2$	3 M KOH	1	2300.8	13
Zn–Ni–P–S	3 M KOH	2	2950 (1180 C g-1)	This work
		10	2327.5 (931 C g-1)	
		20	1950 (780 C g-1)	

Table S2.The comparison of Coulomb efficiency (CE) under different current densities

Current density (A g^{-1})	**2**	**3**	**4**	**5**	**10**	**20**
CE of ZNPS (%)	86.76	90.86	92.48	93.96	94.90	96.30
CE of ZNP (%)	92.74	96.36	96.88	96.48	98.32	98.94
CE of ZNS (%)	89.68	93.21	94.96	95.85	97.24	98.33

Table S3. The equivalent circuit impedance parameters fitted from Nyquist plots

Impedance values	**R_{ESR} (Ω)**	**R_{ct} (Ω)**	**W (Ω)**
ZNPS	0.5153	0.08937	0.4935
ZNP	0.6553	0.1304	0.6527
ZNS	0.5970	0.1181	0.5170

References

1 R. Ding, X. Li, W. Shi, Q. Xu, E. Liu, *Chem. Eng. J.*, 2017, **320**, 376–388.

2 L. Shen, L. Yu, H. B. Wu, X.-Y. Yu, X. Zhang & X. W. D. Lou, *Nat. Commun*, 2015, **6**, 6694.

3 Y. Liu, G. Liu, X. Nie, A. Pan, S. Liang, T. Zhu, *J. Mater. Chem. A*, 2019, **7**, 11044–11052.

4 Y. Zhang, Y. Zhang, Y. Zhang, H. Si, L. Sun, *Nano-Micro Lett.*, 2019, 11:35.

5 Y. Shao, Y. Zhao, H. Li, C. Xu, *ACS Appl. Mater. Interfaces*, 2016, **8**, 35368−35376.

6 W. He, C. Wang, H. Li, X. Deng, X. Xu, T. Zhai, *Adv. Energy Mater.*, 2017, **7**, 1700983.

7 H. Tong, W. Bai, S. Yue, Z. Gao, L. Lu, L. Shen, S. Dong, J. Zhu, J. He, X, Zhang, *J. Mater. Chem. A*, 2016, **4**, 11256−11263.

8 X. Li, H. Wu, A. M. Elshahawy, L. Wang, S. J. Pennycook, C. Guan, J. Wang, *Adv. Funct. Mater.*, 2018, 28, **20**, 1800036.

9 J. Yang, C. Yu, X. Fan, S. Liang, S. Li, H. Huang, Z. Ling, C. Hao, J. Qiu, *Energy Environ. Sci*. 2016, **9**, 1299–1307.

10 H. Liang, J. Lin, H. Jia, S. Chen, J. Qi, J. Cao, T. Lin, W. Fei, J. Feng, *J. Mater. Chem. A*, 2018, **6**, 15040–15046.

11 X. Zhang, A. Wu, X. Wang, C. Tian, R. An, H. Fu, *J. Mater. Chem. A*, 2018, **6**, 17905–17914.

12 F. Lu, M. Zhou, L. Wang, Q. Weng, C. Li, Y. Xue, X. Jiang, X. Zeng, Y. Bando, D. Golberg, *Nano Energy*, 2016, **26**, 313–323.

13 Q. Zong, H. Yang, Q. Wang, Q. Zhang, Y. Zhu, H. Wang, Q. Shen, *Chem. Eng. J.*, 2019, **361**, 1–11.